

Determination of crystal structure and physical properties of Ru₂Al₅ intermetallic from first-principles calculations

Jing Luo^a, Meiguang Zhang^{b,*}, Xiaofei Jia^a, Xuanmin Zhu^c, Qun Wei^{a,*}

^a*School of Physics, Xidian University, Xi'an 710071, China*

^b*College of Physics and Optoelectronic Technology, Baoji University of Arts and Sciences, 721016 Baoji, China*

^c*School of Information, Guizhou University of Finance and Economics, Guiyang 550025, China*

ABSTRACT

Novel ordered intermetallic compounds have stimulated much interest. Ru–Al alloys are a prominent class of high-temperature structural materials, but the experimentally reported crystal structure of the intermetallic Ru₂Al₅ phase remains elusive and debatable. To resolve this controversy, we extensively explored the crystal structures of Ru₂Al₅ using first-principles calculations combined with crystal structure prediction technique. Among the calculated X-ray diffraction patterns and lattice parameters of five candidate Ru₂Al₅ structures, those of the orthorhombic *Pmmn* structure best aligned with recent experimental results. The structural stabilities of the five Ru₂Al₅ structures were confirmed through formation energy, elastic constants, and phonon spectrum calculations. We also comprehensively analyzed the mechanical and electronic properties of the five candidates. This work can guide the exploration of novel ordered intermetallic compounds in Ru–Al alloys.

Keywords: Crystal structure, Mechanical properties, First-principles calculations

* Corresponding authors.

E-mail addresses: zhmgbj@126.com (M. Zhang), qunwei@xidian.edu.cn (Q. wei)

Introduction

Ru–Al alloys have attracted considerable interest as advanced high-temperature materials with superior thermodynamic properties, strong oxidation and corrosion resistance, high melting points, and high mechanical strength [1-4]. Lu and Pollock [5] studied the ductility and deformation behaviors of Ru-Al alloys in five independent slip systems at room temperature. Since the pioneering studies of Obrowski, who characterized intermetallic Ru-Al using optical microscopy, X-ray diffraction (XRD) analysis, and thermal studies [6,7], the phase diagram of Ru-Al alloys has been experimentally modified and updated [8-10]. Prins *et al.* [11] conducted a theoretical study of Ru-Al alloys, obtaining results consistent with the experimental findings. Five intermetallic compounds have been consensually identified in the Ru-Al binary system: RuAl, Ru₂Al₃, RuAl₂, Ru₄Al₁₃, and RuAl₆. Using multiple measurement methods and techniques, Mi *et al.* [12] re-examined the Al-rich region of the Ru-Al phase diagram, revealing an orthorhombic Ru₂Al₅ intermetallic phase formed at 1492 °C via a peritectic reaction of RuAl₂ with the liquid. However, the atomic positions of this new Ru₂Al₅ phase could not be precisely determined from the inexact XRD profiles, so only the lattice parameters were provided. Accordingly, the Ru₂Al₅ intermetallic phase was assumed to be isostructural to Fe₂Al₅ (*Cmcm*, *Z*= 2). Using an alternative mechanical alloying and subsequent heat treatment, Bai *et al.* [13] prepared the mother alloy Al₇₉:Ru₂₁ of a skeletal Ru catalyst. They reported that the Ru₂Al₅ phase appeared in all samples after heat treatment at 550 °C and disappeared after 2 h of heat treatment at 700 °C. Despite these efforts, the atomic sites of Ru₂Al₅ remain uncharacterized. Motivated by previous experimental works [12,13], Wen *et al.* [14] analyzed six Ru-Al intermetallic compounds using first-principles calculations. However, the calculated lattice constants of the supposed Fe₂Al₅-type Ru₂Al₅ intermetallic phase deviated from recent experimental results [12]. A subsequent theoretical study proposed a hexagonal *P6₃/mmc*-Ru₂Al₅ [15]. As clarifying structure of Ru₂Al₅ is essential for properly understanding Ru-Al alloys, we conducted a systematic crystal structure search of Ru₂Al₅ using the particle swarm optimization (PSO) algorithm in CALYPSO code [16-18]. Among several candidate Ru₂Al₅ structures identified by the search algorithm, the orthorhombic *Pmnm* structure most favorably agreed with the available experimental data. The structural stabilities and mechanical and thermodynamic properties of the obtained Ru₂Al₅ structures were systematically analyzed.

Computational methods

The PSO algorithm is the global optimization technique used in CALYPSO. By updating the positions of particles based on both individual and collective optimal solutions, the PSO algorithm effectively explores complex search spaces to predict stable and metastable crystal structures [16]. The CALYPSO code has successfully predicted the crystal structures of various systems [19-23]. In the present study, the energetically favorable structures of Ru_2Al_5 , were identified through variable-cell crystal structure simulations of Ru_2Al_5 at 0 GPa. During the structure search, the population size was set to 50 in each generation, and the first generation was randomly generated under symmetry constraints. Thirty generations were set to achieve convergence. Once the structure search had terminated, the energetically stable structures were retained for further structural relaxations and related property simulations in the Vienna *Ab initio* Simulation Package [24]. The generalized gradient approximation was adopted for the projector-augmented wave ion–electron potentials [25] and the Perdew–Burke–Ernzerhof exchange–correlation functional [26]. A 400 eV cutoff was set for the plane wave expansion and the grid spacing of the Monkhorst–Pack k meshes [27] was $2\pi \times 0.04 \text{ \AA}^{-1}$ to ensure good convergence of the total energy ($1 \times 10^{-5} \text{ eV/atom}$). The single-crystal elastic constants were deduced from the strain–stress relations [28]. The polycrystalline elastic moduli were calculated by the Voigt–Reuss–Hill averaging method [29]. The dynamic stabilities were evaluated from the phonon spectra obtained in PHONOPY code, employing the finite displacement method [30].

Results and discussion

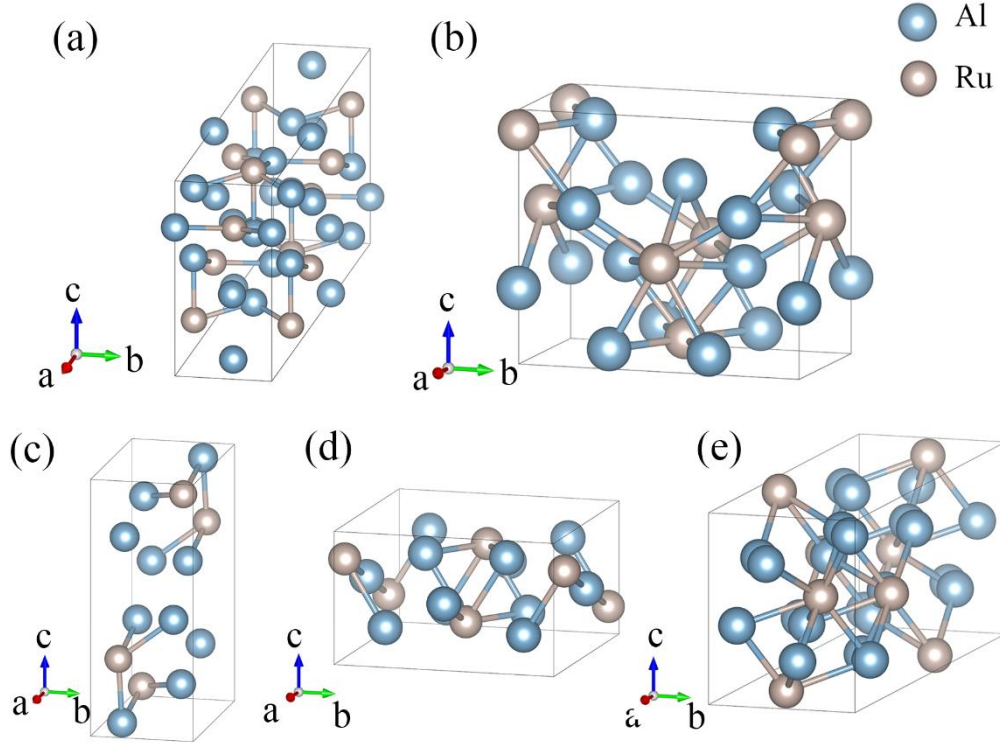


Fig. 1. Crystal structures of the (a) $C2/m-1$, (b) $Pmmn$, (c) $P2_1/m$, (d) $C2/m-2$, and (e) $C2/c$ phases of Ru_2Al_5 .

The crystal structures were comprehensively searched at ambient pressure using CALYPSO code. The search obtained five energetically stable Ru_2Al_5 structures, one orthorhombic and four monoclinic phases (Fig. 1). In the $C2/m-1$ phase, the Al and Ru atoms are linearly arranged along the [010] and [110] directions. Along the [001] direction and two arrangements appear along the [001] direction: an alternating sequence of two Al atoms and one Ru atom and a linear sequence of Al atoms. The $P2_1/m$ phase presents two types of zigzag chains along the [100] direction: a chain of alternating Al and Ru atoms and a chain comprised only Al atoms. Along the [100] and [010] directions of the $Pmmn$ phase, both the Al and Ru atoms are arranged in straight lines. In the $C2/m-2$ phase, the Al and Ru atoms are arranged in straight lines along the three principal axes. Table 1 lists the lattice constants and atomic positions of the Ru_2Al_5 structures at ambient pressure after full structural relaxations. The lattice constants of the discovered $Pmmn$ phase ($a = 4.235 \text{ \AA}$, $b = 7.612 \text{ \AA}$, and $c = 6.637 \text{ \AA}$) are remarkably consistent with the experimental data provided by Mi *et al.* ($a = 4.2 \text{ \AA}$, $b = 7.8 \text{ \AA}$, and $c = 6.6 \text{ \AA}$) [12]. The thermodynamic stability of each Ru_2Al_5 intermetallic phase was determined from the formation energy (ΔH) [31] of each phase as follows:

$$\Delta H = [E(Ru_2Al_5) - 2E(Ru) - 5E(Al)]/7, \quad (1)$$

Herein, $E(\text{Ru}_2\text{Al}_5)$ denotes the total free energy of each structure at 0 K, and $E(\text{Ru})$ and $E(\text{Al})$ represent the energies of Ru and Al atoms in metals, respectively. Here, we also considered the previously proposed $Cmcm$ Fe_2Al_5 -type and hexagonal $P6_3/mmc$ phases [12,15] of Ru_2Al_5 . The ΔH values of all structures are negative (Fig. 2), suggesting that they are thermodynamically stable and potentially synthesizable. The $Pm\bar{m}n$ phase has the second lowest energy among the considered structures and a lower energy than the earlier reported Fe_2Al_5 -type and $P6_3/mmc$ phases. Therefore, the discovered $Pm\bar{m}n$ structure is probably the actual structure of Ru_2Al_5 reported in previous experimental works [12,13]. Fig. 3 plots the phonon spectra of the five Ru_2Al_5 structures. The eigenfrequencies of the lattice vibrations in the Brillouin zone of each structure are positive at ambient pressure, indicating the dynamic stability.

Table 1

Space group (SG), lattice parameters, and atomic Wyckoff positions of the five new Ru_2Al_5 phases.

| SG | Lattice parameters | | | | Atomic Wyckoff positions | |
|--------------|--------------------|---------|---------|-------------|--|--|
| | a (Å) | b (Å) | c (Å) | β (°) | Al | Ru |
| $C2/m-1$ | 13.119 | 4.126 | 7.990 | 106.1 | $4i$ (0.999, 0.0, 0.761) $4i$ (0.589, 0, 0.631, 0.631) $4i$ (0.899, 0.5, 0.028) $4i$ (0.689, 0.5, 0.528) $4i$ (0.696, 0.5, 0.177) | $4i$ (0.805, 0.0, 0.150) $4i$ (0.891, 0.5, 0.693) |
| $Pm\bar{m}n$ | 4.235 | 7.613 | 6.637 | | $4e$ (0.5, 0.713, 0.376) $4e$ (0.0, 0.322, 0.078) $2a$ (0.0, 0.0, 0.299) | $2a$ (0.0, 0.0, 0.919) $2b$ (0.0, 0.5, 0.424) |
| $P2_1/m$ | 5.086 | 4.138 | 9.968 | 98.9 | $2e$ (0.855, 0.750, 0.446) $2e$ (0.510, 0.750, 0.621) $2e$ (0.673, 0.750, 0.167) $2e$ (0.141, 0.750, 0.964) $2e$ (0.797, 0.250, 0.749) | $2e$ (0.620, 0.750, 0.898) $2e$ (0.055, 0.750, 0.703) |
| $C2/m-2$ | 6.724 | 7.536 | 4.380 | 92.9 | $8j$ (0.661, 0.685, 0.756) $2d$ (0.5, 0.0, 0.5) | $4i$ (0.163, 0.0, 0.259) |
| $C2/c$ | 14.506 | 4.699 | 5.910 | 90.5 | $8f$ (0.718, 0.379, 0.819) $8f$ (0.923, 0.885, 1.384) $4e$ (0.0, 0.607, 0.750) | $8f$ (0.856, 0.283, 0.529) |

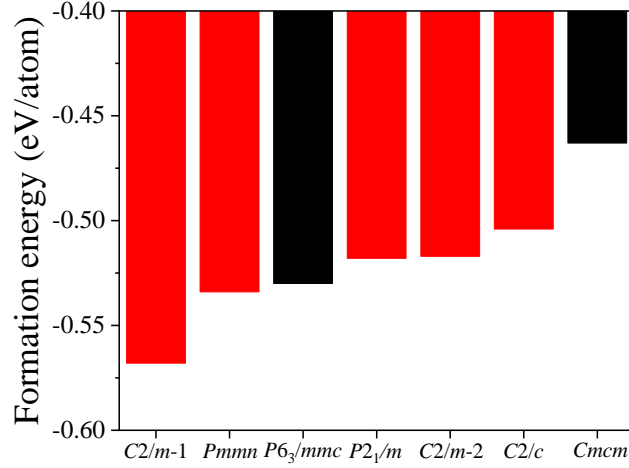


Fig. 2. Calculated formation energies of different Ru₂Al₅ phases. Red bars represent the five new phases.

Inspired by the perfect consistency between the predicted and experimental lattice constants of the *Pmmn* phase and the energy advantage of *Pmmn* phase over the previously proposed Fe₂Al₅-type and *P6₃/mmc* phases, we further confirmed the *Pmmn* phase of Ru₂Al₅. To this end, we compared the XRD patterns of this *Pmmn* phase and that obtained in recent experiments. The simulated and experimental XRD patterns of the *Pmmn* structure are presented in Fig. 4. Our simulations adopted Cu-*K*α radiation for consistency with earlier experiments. The obtained main peaks of the *Pmmn* structure almost coincided with the experimental data, implying that the experimental phase is indeed the *Pmmn* phase [12]. It should be noted that a lower-energy stable structure (*C2/m-1* phase; Fig. 2) was also identified. Therefore, if the Ru₂Al₅ structure of the *Pmmn* phase is the Ru₂Al₅ structure synthesized by Mi *et al.* [12], then *Pmmn* phase is likely a metastable phase.

The elastic parameters are fundamental for understanding the mechanical performances of Ru-Al intermetallic phases. The elastic constants C_{ij} of the five Ru₂Al₅ structures are listed in Table 2. A necessary condition of crystal stability is mechanical stability. For monoclinic systems (*C2/m-1*, *P2₁/m*, *C2/m-2*, and *C2/c*) and the orthorhombic *Pmmn* structure, mechanical stability can be assessed under mechanical stability criteria [32-34]. Based on our calculations, all five structures met the criteria, confirming their mechanical stability. The elastic constants of *C2/m-1* and *Pmmn* trend as: $C_{11} < C_{22} \approx C_{33}$ and $C_{11} > C_{22} = C_{33}$, respectively, indicating lower anisotropy of axial incompressibility in these structures than in the other candidate structures. C_{44} and C_{66} refer to the shear-resistance deformations under a shear stress along the $\langle 001 \rangle$ direction of the (100) plane and

under a shear load along the $\langle 110 \rangle$ direction of the (100) plane, respectively. As $C_{44} > C_{66}$ in both the $Pmmn$ and $C2/c$ phases, the shear modulus of deformation is larger along the $\langle 001 \rangle$ direction than along the $\langle 110 \rangle$ direction of (100) plane. In the remaining three structures, $C_{44} < C_{66}$, implying opposite shear behaviors on the (100) plane.

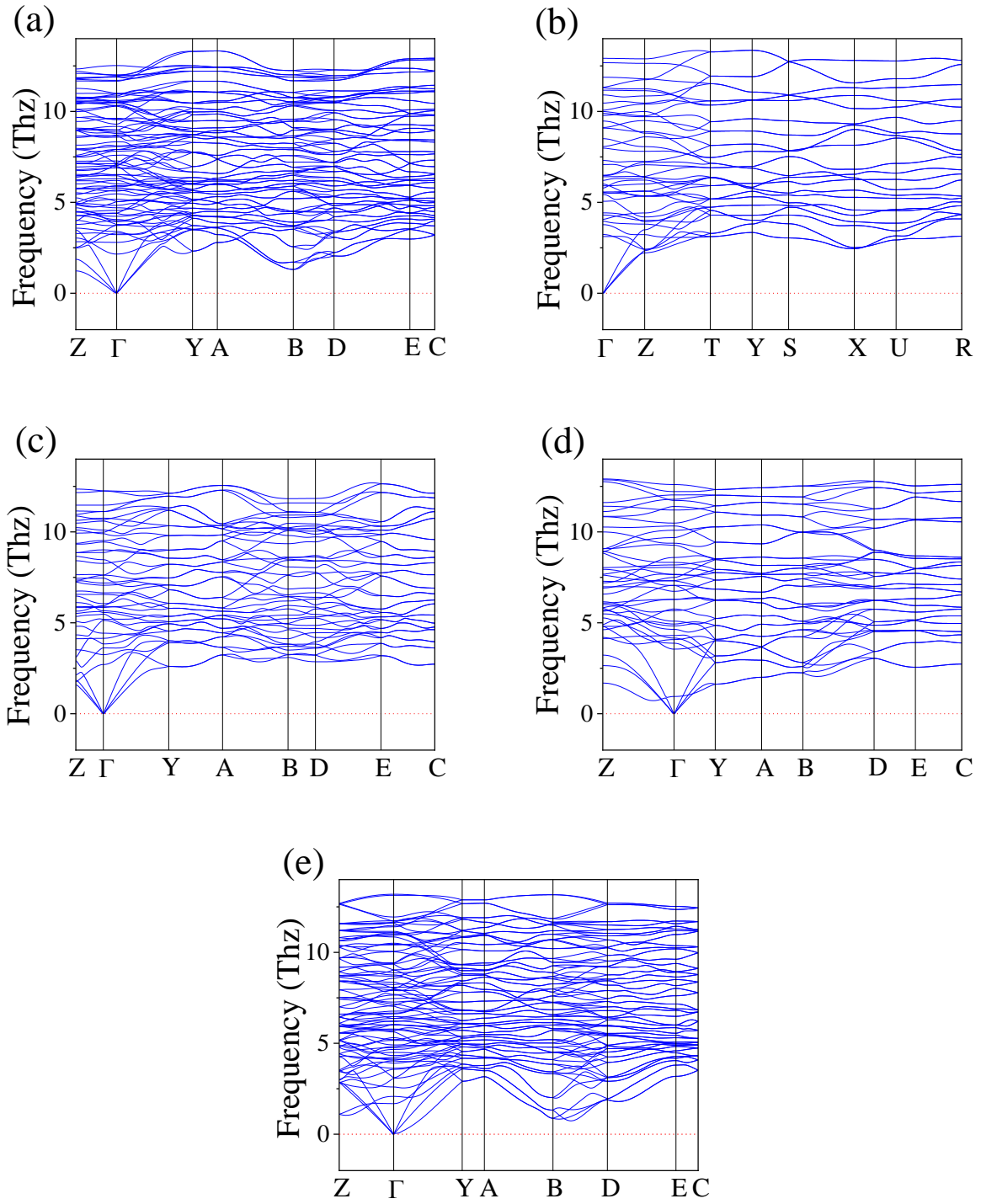


Fig. 3. Phonon spectra of the (a) $C2/m-1$, (b) $Pmmn$, (c) $P2_1/m$, (d) $C2/m-2$, and (e) $C2/c$ phases of Ru_2Al_5 .

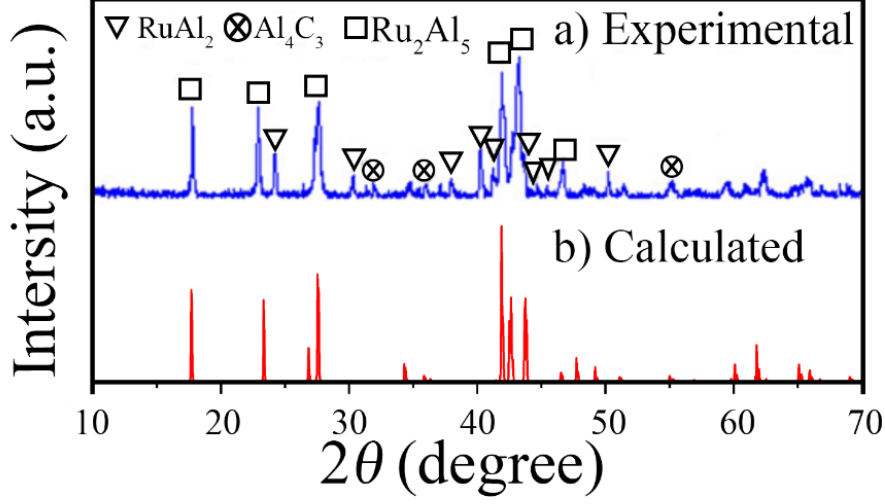


Fig. 4. (a) XRD patterns of milled and heat treated $\text{Al}_{79}\text{Ru}_{21}$ powders and (b) simulated XRD pattern of the $Pmmn$ structure. The experiment and calculation adopted the same wavelength of the light source (1.54 \AA).

Table 2.

Calculated elastic constants C_{ij} (GPa) of the five Ru_2Al_5 phases.

| Phases | C_{11} | C_{22} | C_{33} | C_{44} | C_{55} | C_{66} | C_{12} | C_{13} | C_{15} | C_{23} | C_{25} | C_{35} | C_{46} |
|----------|----------|----------|----------|----------|----------|----------|----------|----------|----------|----------|----------|----------|----------|
| $C2/m-1$ | 251 | 275 | 274 | 76 | 49 | 107 | 127 | 60 | -6 | 6 | 32 | -31 | -2 |
| $Pmmn$ | 266 | 234 | 234 | 90 | 80 | 87 | 104 | 56 | | 90 | | | |
| $P2_1/m$ | 248 | 288 | 225 | 66 | 92 | 105 | 104 | 61 | -19 | 77 | 5 | -2 | 8 |
| $C2/m-2$ | 247 | 230 | 240 | 68 | 66 | 91 | 75 | 62 | 28 | 112 | 8 | 26 | 19 |
| $C2/c$ | 208 | 298 | 225 | 74 | 76 | 23 | 87 | 125 | -23 | 65 | 7 | -1 | -25 |

The mechanical properties of a polycrystalline material under different deformation conditions largely depend on the elastic moduli of the material, represented by the bulk modulus (B), Young's modulus (E), and shear modulus (G). Elucidating the elastic moduli is critical for designing and selecting materials to meet specific engineering needs. The bulk and shear moduli of the monoclinic and orthorhombic structures were calculated using the Voigt-Reuss-Hill approach [29]. The Young's modulus (E) and Poisson's ratio (ν) are determined as follows:

$$B_V = \frac{1}{9}(C_{11} + C_{22} + C_{33}) + \frac{2}{9}(C_{12} + C_{13} + C_{23}), \quad (2)$$

$$G_V = \frac{1}{15}(C_{11} + C_{22} + C_{33} - C_{12} - C_{13} - C_{23}) + \frac{1}{5}(C_{44} + C_{55} + C_{66}), \quad (3)$$

$$B_R = [(s_{11} + s_{22} + s_{33}) + 2(s_{12} + s_{13} + s_{23})]^{-1}, \quad (4)$$

$$G_R = 15[4(s_{11} + s_{22} + s_{33}) - 4(s_{12} + s_{13} + s_{23}) + 3(s_{44} + s_{55} + s_{66})]^{-1}, \quad (5)$$

$$B = \frac{1}{2}(B_V + B_R), \quad (6)$$

$$G = \frac{1}{2}(G_V + G_R), \quad (7)$$

$$E = \frac{9BG}{3B+G}, \quad (8)$$

$$\nu = \frac{3B-2G}{6B+2G}, \quad (9)$$

where the s_{ij} are the elastic compliance constants. The subscripts V and R represent the Voigt and Reuss approximations, respectively. Table 3 lists the calculated elastic moduli and Poisson's ratios of the five Ru_2Al_5 structures. The B/G value evaluates the brittleness or ductility of a material and can also indicate bonding type [35]. Studies have shown that a change in bonding type induces a ductility-to-brittleness transition in materials [36]. A material with a B/G below 1.75 is generally considered as brittle, whereas a material with B/G above 1.75 is typically ductile and can withstand large plastic deformation before breaking. The $P2_1/m$ and $Pmnm$ phases are brittle, as evidenced by their B/G ratio below 1.75, indicating high hardness and breakage at low plastic deformation under an external force. The remaining three monoclinic structures have large B/G ratios (>1.75), clarifying their ductile behaviors and high resistance to stress fracture. Hardness is closely related to the shear modulus and Poisson's ratio of a material. Materials with high hardness have high shear moduli, meaning that their dislocation movement is limited and occurs only under a high shear stress. Meanwhile, materials with a low Poisson's ratio exhibit small lateral contraction when stretched, this phenomenon is often related to directional bonds in the material. A low Poisson's ratio enhances the shear modulus by limiting the lateral expansion under shear. The large shear moduli (86 and 83 GPa, respectively) and small Poisson's ratios (0.240 and 0.248, respectively) of the $P2_1/m$ and $Pmnm$ phases (Table 3) suggest high hardness of these structures. According to Chen's hardness model, the Vickers hardness values [37] of materials is given by $H_V = (2k^2G)^{0.585} - 3$, where $k = G/B$. The $P2_1/m$ and $Pmnm$ phases possess large hardness values (12.6 and 11.6 GPa, respectively).

Elastic anisotropy is an important property of crystals in practical applications. For example, the elastic anisotropy of piezoelectric fiber composites (piezocomposites) is exploited in various aerospace applications, including active vibration control systems, adaptive blades, and flexible morphing wings [38]. The direction-dependent Young's moduli of the candidate Ru_2Al_5 structures are plotted in Fig. 5. An ideally isotropic material yields a spherical Young's modulus diagram. If the Young's modulus pattern deviates from a sphere, the material is harder or softer in one or more directions. The Young's modulus in a certain direction can be determined by measuring the distance

from the origin of the coordinate system to a corresponding point on the surface. As demonstrated in Fig. 5, the five Ru_2Al_5 structures are elastically anisotropic, although the $Pm\bar{m}n$ structure of Ru_2Al_5 shows smaller elastic anisotropy than the other candidates.

Table 3

Calculated bulk moduli B (GPa), shear moduli G (GPa), Young's moduli E (GPa), B/G ratios, Poisson's ratios ν , and hardness values (GPa) of Ru_2Al_5 .

| Phases | B | G | E | B/G | ν | H_V |
|--------------|-----|-----|-----|-------|-------|-------|
| $C2/m-1$ | 145 | 74 | 190 | 1.95 | 0.281 | 8.3 |
| $Pm\bar{m}n$ | 137 | 83 | 207 | 1.65 | 0.248 | 11.6 |
| $P2_1/m$ | 136 | 86 | 212 | 1.59 | 0.240 | 12.6 |
| $C2/m-2$ | 131 | 73 | 186 | 1.79 | 0.264 | 9.4 |
| $C2/c$ | 142 | 51 | 136 | 2.81 | 0.341 | 3.6 |

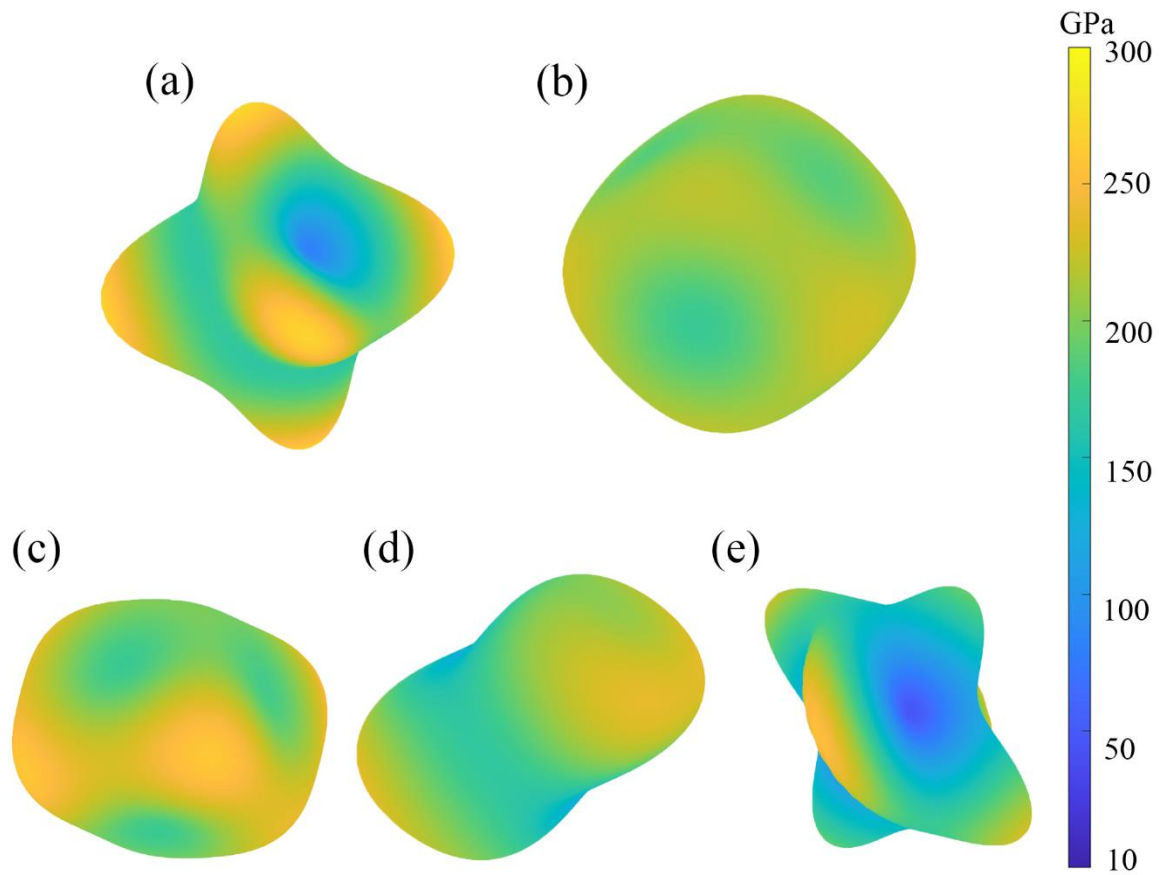


Fig. 5. Directional dependence of Young's moduli of the (a) $C2/m-1$, (b) $Pm\bar{m}n$, (c) $P2_1/m$, (d) $C2/m-2$, and (e) $C2/c$ phases of Ru_2Al_5 .

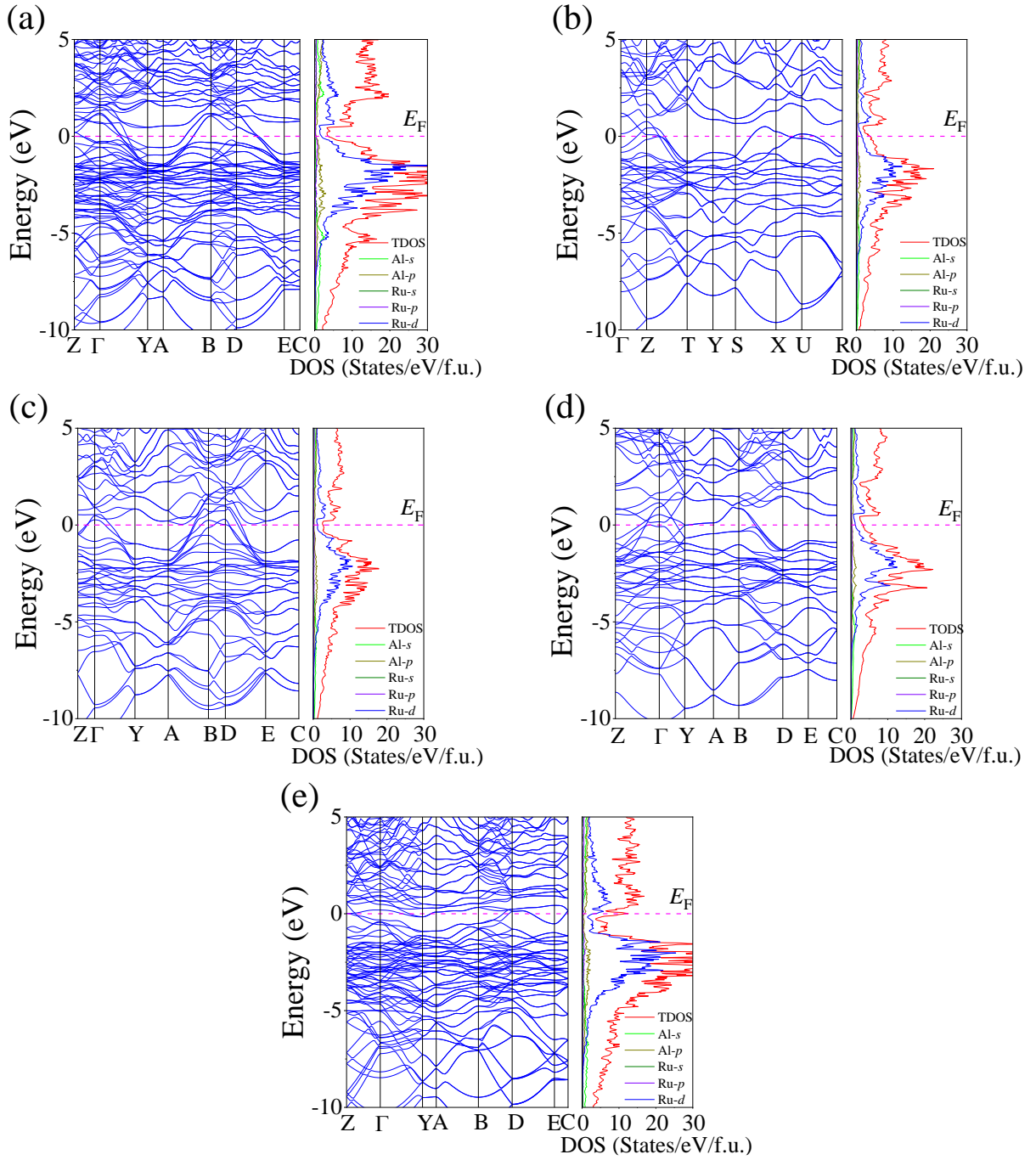


Fig. 6. Calculated band structures and the densities of stats of the (a) $C2/m-1$, (b) $Pmmn$, (c) $P2_1/m$, (d) $C2/m-2$, and (e) $C2/c$ phases of Ru_2Al_5 . Dashed lines represent the Fermi levels.

Fig. 6 plots the electronic energy bands and densities of states (DOSs) of the five Ru_2Al_5 structures. The valence band intersects the Fermi level with no band gap, indicating that electrons at the Fermi level can move freely through the conduction band. As the current flow is not restricted by a band gap, the five Ru_2Al_5 structures are electrically conductive, indicating that they are metallic compounds. Further examination of the atomic DOS shows that the Ru-*d* orbital electrons play a major role in the metallic properties of Ru_2Al_5 . In addition, the total DOSs of all five structures feature

a sharp valley around the Fermi level (known as a pseudogap), indicating the energy separation between the bonding and antibonding states. Earlier works [39-41] suggested that pseudogaps in DOSs indicate strong hybridization between the orbitals of the different atoms in a crystal structure, which contribute to structural stability. Clearly, the bonding states are nearly filled with the Fermi level around the pseudogap, underlying the structural stability of the Ru₂Al₅ compounds.

To determine the chemical bonding in the five Ru₂Al₅ compounds, we plot their charge-density distributions in Fig. 7. All structures exhibit regions of electron depletion and accumulation between the Al and Ru atoms, where ionic bonds are formed. Uneven chemical bond distribution affects the directionality, strength, bond lengths, and bond angles of the chemical bonds, thereby influencing the local stress state and symmetry of the crystal structure, and causing directional variations in the Young's modulus. The different elastic responses of the material in different directions ultimately manifest as an anisotropic Young's modulus. For example, the Young's modulus of *C2/m-1* is strongly anisotropic along three main directions where the ionic bonds are concentrated. In the differential charge-density map of the *Pmmn* structure, the absolute values of charge density are considerably smaller along the (1 0 1), (1 0 -1), and (0 1 0) directions than along the (1 1 0), (1 -1 0), (0 1 1), and (0 1 -1) directions. Consequently, the three-dimensional Young's modulus is cubic with a 45° angle between the line connecting the centroid and the origin and the (0 0 1) plane.

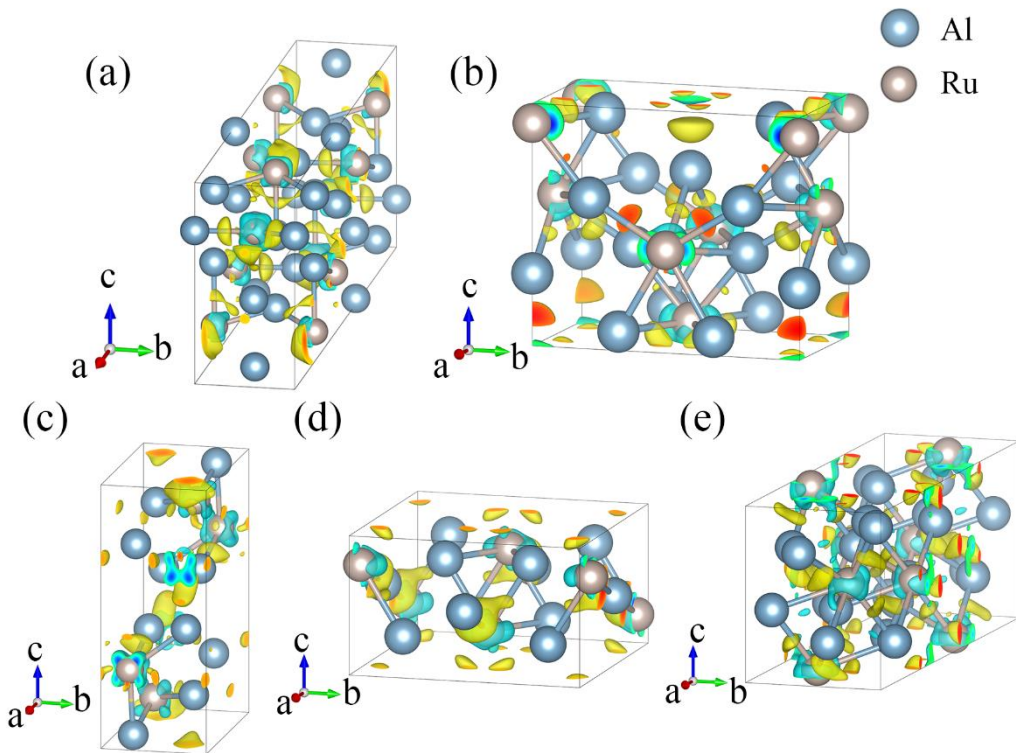


Fig. 7. Charge-density differences in the (a) $C2/m-1$, (b) $Pmmn$, (c) $P2_1/m$, (d) $C2/m-2$, and (e) $C2/c$ phases of Ru_2Al_5 . The blue and brown spheres represent Al and Ru atoms, respectively. Blue and yellow regions indicate electron depletion and accumulation, respectively.

Conclusion

To solve the long-missing crystal structure of the experimentally synthesized Ru_2Al_5 intermetallic phase in Ru-Al alloys, we extensively searched the space of crystal structures using swarm intelligence structure simulations combined with first-principles calculations. Among the five stable phases of Ru_2Al_5 obtained by the search, the orthorhombic $Pmmn$ structure yielded a calculated XRD spectra and lattice parameters that aligned well with the experimental data. Thus, the experimental phase of Ru_2Al_5 was confirmed as the $Pmmn$ phase. The brittle/ductile behavior, elastic anisotropy, and ionic bonding of each Ru_2Al_5 candidate structure were demonstrated through elastic and electronic structural calculations.

CRedit authorship contribution statement

Jing Luo: Investigation, Data curation, Writing – original draft. **Meiguang Zhang:** Resources, Funding acquisition. Writing – review & editing. **Xiaofei Jia:** Investigation, Data curation. **Xuanmin Zhu:** Investigation. **Qun Wei:** Supervision, Project administration, Writing – review & editing.

Declaration of competing interest

The authors declare that they have no known competing financial interests or personal relationships that could have appeared to influence the work reported in this paper.

Data availability

Data will be made available on request.

Acknowledgments

This work was financially supported by the National Natural Science Foundation of China (Grant Nos.: 11965005 and 11964026), the Natural Science Basic Research plan in Shaanxi Province of China (Grant Nos.: 2023-JC-YB-021, 2022JM-035), the Fundamental Research Funds for the Central Universities, and the 111 Project (B17035). All the authors thank the computing facilities at High Performance Computing Center of Xidian University.

References

- [1] Guitar MA, Ramos-Moore E, F. Mücklich. The influence of impurities on the formation of protective aluminium oxides on RuAl thin films. *J Alloys Compd* 2014;594:165. <https://doi.org/10.1016/j.jallcom.2014.01.137>
- [2] Zhang Z, Bai B, Peng H, Gong S, Guo H. Effect of Ru on interdiffusion dynamics of β -NiAl/DD6 system: A combined experimental and first-principles studies. *Mater Design* 2015;88:667. <https://doi.org/10.1016/j.matdes.2015.09.041>
- [3] Guitar MA, Mücklich F. Isothermal oxidation behaviour of nanocrystalline RuAl intermetallic thin films. *Oxid Met* 2013;80:423. <https://doi.org/10.1007/s11085-013-9409-8>
- [4] Bidabad ARS, Enayati MH, Dastanpoor E, Varin RA, Biglari M. Nanocrystalline intermetallic compounds in the Ni-Al-Cr system synthesized by mechanical alloying and their thermodynamic analysis. *J Alloys Compd* 2013; 581:91. <https://doi.org/10.1016/j.jallcom.2013.07.037>
- [5] Lu DC, Pollock TM. Low temperature deformation and dislocation substructure of ruthenium aluminide polycrystals. *Acta Mater* 1999;47:1035. [https://doi.org/10.1016/S1359-6454\(98\)00359-0](https://doi.org/10.1016/S1359-6454(98)00359-0)
- [6] Obrowski W. B2-fasen von aluminium mit T-metallen der VII. und VIII. Gruppe des periodischen systems. *Naturwissenschaften* 1960;47:14. <https://doi.org/10.1007/BF00628450>
- [7] Obrowski W. Alloys of ruthenium with boron, beryllium and aluminum. *Metall (Berlin)*, 1963;17:108. <https://www.osti.gov/biblio/4730033>
- [8] Anlage SM, Nash P, Ramachandran R, Schwarz RB. Phase equilibria for the aluminum-rich region of the Al-Ru system. *J Less-Common Met* 1988;136:237. [https://doi.org/10.1016/0022-5088\(88\)90427-4](https://doi.org/10.1016/0022-5088(88)90427-4)
- [9] Boniface TD, Cornish LA. Investigation of the high aluminium end of the aluminium-ruthenium phase diagram. *J Alloys Compd* 1996;233:241. [https://doi.org/10.1016/0925-8388\(95\)01934-0](https://doi.org/10.1016/0925-8388(95)01934-0)
- [10] Boniface TD, Cornish LA. Investigation of the aluminium-ruthenium phase diagram above 25 at.% ruthenium. *J Alloys Compd*, 1996;234:275. [https://doi.org/10.1016/0925-8388\(95\)01933-2](https://doi.org/10.1016/0925-8388(95)01933-2)

- [11] Prins SN, Cornish LA, Stumpf WE, Sundman B. Thermodynamic assessment of the Al-Ru system. *Calphad* 2003;27:79. [https://doi.org/10.1016/S0364-5916\(03\)00033-6](https://doi.org/10.1016/S0364-5916(03)00033-6)
- [12] Mi S, Balanetsky S, Grushko B. A study of the Al-rich part of the Al–Ru alloy system. *Intermetallics*, 2003;11:643. [https://doi.org/10.1016/S0966-9795\(03\)00052-9](https://doi.org/10.1016/S0966-9795(03)00052-9)
- [13] Bai F, Chai ZX, Qi K, Li TL, Lu LH. Study on Ru₂Al₅ prepared by mechanical alloying and subsequent heat treatment. *J Alloys Compd*, 2009;486:801. <https://doi.org/10.1016/j.jallcom.2009.07.069>
- [14] Wen B, Zhao J, Bai F, Li T. First-principle studies of Al–Ru intermetallic compounds. *Intermetallics*, 2008;16:333. <https://doi.org/10.1016/j.intermet.2007.11.003>
- [15] Pan Y, Zhu J, Luo J. Role of Ru concentration on structure, mechanical and thermodynamic properties of Ru-Al compounds. *Mater Design*, 2017;118:146. <https://doi.org/10.1016/j.matdes.2017.01.049>
- [16] Wang Y, Lv J, Zhu L, Ma Y, CALYPSO: A method for crystal structure prediction. *Comput Phys Commun* 2012;183:2063. <https://doi.org/10.1016/j.cpc.2012.05.008>
- [17] Tong Q, Lv J, Gao P, Wang Y. The CALYPSO methodology for structure prediction. *Chin Phys B* 2019;28:106105. <https://doi.org/10.1088/1674-1056/ab4174>
- [18] Wang Y, Lv J, Zhu L, Ma Y. Crystal structure prediction via particle-swarm optimization. *Phys Rev B* 2010;82:094116. <https://doi.org/10.1103/PhysRevB.82.094116>
- [19] Duan Q, Shen J, Zhong X, Lu H, Lu C. Structural phase transition and superconductivity of ytterbium under high pressure. *Phys Rev B* 2022;105:214503. <https://doi.org/10.1103/PhysRevB.105.214503>.
- [20] Xie X, Wei Q, Jia X, Zhang M, Wu Z, Zhu X. Pressure-induced phase transformation and mechanical stability of HfAl₂. *Comput Theor Chem* 2024;1234:114537. <https://doi.org/10.1016/j.comptc.2024.114537>
- [21] Yan H, Chen L, Feng L, Chen Y, Zhang M, Wei Q. Two dense semiconducting phases of LiInTe₂ under high pressure. *Vacuum*. 2024;225:113256. <https://doi.org/10.1016/j.vacuum.2024.113256>
- [22] Lu C, Cui C, Zuo J, Zhong H, He S, Dai W, Zhong X. Monolayer ThSi₂N₄: An indirect-gap semiconductor with ultra-high carrier mobility. *Phys Rev B* 2023;108:205427. <https://doi.org/10.1103/PhysRevB.108.205427>

- [23] Duan Q, Zhan L, Shen J, Zhong X, Lu C. Predicting superconductivity near 70 K in 1166-type boron-carbon clathrates at ambient pressure. *Phys Rev B* 2024;109:054505.
<https://doi.org/10.1103/PhysRevB.109.054505>
- [24] Kresse G, Furthmüller J. Efficient iterative schemes for ab initio total-energy calculations using a plane-wave basis set. *Phys Rev B* 1996;54:11169.
<https://doi.org/10.1103/PhysRevB.54.11169>
- [25] Kresse G, Joubert D. From ultrasoft pseudopotentials to the projector augmented-wave method. *Phys Rev B* 1999;59:1758. <https://doi.org/10.1103/PhysRevB.59.1758>
- [26] Perdew JP, Burke K, Ernzerhof M. Generalized Gradient Approximation Made Simple. *Phys Rev Lett* 1996;77:3865. <https://doi.org/10.1103/PhysRevLett.77.3865>
- [27] Monkhorst HJ, Pack JD. Special points for Brillouin-zone integrations. *Phys Rev B* 1976;13:5188. <https://doi.org/10.1103/PhysRevB.13.5188>
- [28] Cui Z, Sun Y, Li J, Qu J. Combination method for the calculation of elastic constants. *Phys Rev B* 2007;75:214101. <https://doi.org/10.1103/PhysRevB.75.214101>
- [29] Hill R. The Elastic Behaviour of a Crystalline Aggregate. *Proc Phys Soc A* 1952;65:349.
<https://doi.org/10.1088/0370-1298/65/5/307>
- [30] Togo A, Tanaka I. First principles phonon calculations in materials science. *Scripta Mater* 2015;108:1. <https://doi.org/10.1016/j.scriptamat.2015.07.021>
- [31] Chong XY, Jiang YH, Zhou R, Feng J. First principles study the stability, mechanical and electronic properties of manganese carbides. *Comput Mater Sci* 2014;87:19.
<https://doi.org/10.1016/j.commatsci.2014.01.054>
- [32] Wu Z, Zhao E, Xiang H, Hao X, Liu X, Meng J, Crystal structures and elastic properties of superhard IrN₂ and IrN₃ from first principles. *Phys Rev B* 2007;76:054115.
<https://doi.org/10.1103/PhysRevB.76.054115>
- [33] Mouhat F, Coudert F. Necessary and sufficient elastic stability conditions in various crystal systems. *Phys Rev B* 2014;90:224104. <https://doi.org/10.1103/PhysRevB.90.224104>
- [34] Gao J, Liu Q J, Tang B. Elastic stability criteria of seven crystal systems and their application under pressure: Taking carbon as an example. *J. Appl. Phys.* 2023;133:135901.
<https://doi.org/10.1063/5.0139232>

- [35] Pugh SF, XCII. Relations between the elastic moduli and the plastic properties of polycrystalline pure metals. *Philos Mag* 1954;45:823.
<https://doi.org/10.1080/14786440808520496>
- [36] Sun R, Johnson DD. Stability maps to predict anomalous ductility in B2 materials. *Phys Rev B- Condens. Matter Mater. Phys.* 2013;87:104107.
<https://doi.org/10.1103/PhysRevB.87.104107>
- [37] Chen XQ, Niu H, Li D, Li Y. Modeling hardness of polycrystalline materials and bulk metallic glasses. *Intermetallics* 2011;19:1275. <https://doi.org/10.1016/j.intermet.2011.03.026>
- [38] Wang X, Hu X, Huang C, Zhou W. Multi-mode shape control of active compliant aerospace structures using anisotropic piezocomposite materials in antisymmetric bimorph configuration. *Aerospace* 2022;9:195. <https://doi.org/10.3390/aerospace9040195>
- [39] Xu JH, Freeman AJ. Phase stability and electronic structure of ScAl₃ and ZrAl₃ and of Sc-stabilized cubic ZrAl₃ precipitates. *Phys Rev B* 1990;41:12553.
<https://doi.org/10.1103/PhysRevB.41.12553>
- [40] Zhang M, Wang H, Wang H, Zhang X, Iitaka T, Ma Y. First-principles prediction on the high-pressure structures of transition metal diborides (TMB₂, TM = Sc, Ti, Y, Zr). *Inorg Chem* 2010;49:6859. <https://doi.org/10.1021/ic100214v>
- [41] Ravindran P, Asokamani R, Correlation between electronic structure, mechanical properties and phase stability in intermetallic compounds. *Bull Mater Sci* 1997;20:613.
<https://doi.org/10.1007/BF02744780>